(Received 1 April 2026, Accepted 7 May 2026, Scheduled 27 May 2026)

Structural Optimization of Short Primary Single-Sided Linear Induction Motor

Cheng Wen[1], Zilei Duan[1], Mingye Li[2,*], and Aosai Li[1]

[1] *Hebei Provincial Collaborative lnnovation Center of Transportation Power Grid Intelligent Integration Technology and Equipment School of Electrical and Electronic Engineering, Shijiazhuang Tiedao University, Hebei 050043, China*
[2] *Hebei University of Engineering Science, Shijiazhuang, Hebei 050091, China*

ABSTRACT: This study focuses on a Short-Primary Single-Sided Linear Induction Motor (SSLIM), which is widely used in the rail transit sector due to its low operating noise and small turning radius. Therefore, designing linear induction motors with better performance is of great significance. This study aims to enhance electromagnetic thrust and reduce fluctuations in electromagnetic force by optimizing the motor's structural design. First, a motor model is established based on its operating principles, and a brief analysis of its electromagnetic characteristics is conducted. Second, two design schemes were selected for both the primary and secondary components. For the primary components, one scheme employs a chamfered structure to suppress fluctuations in electromagnetic force, while the other modifies the tooth tip shape from rectangle to trapezoid to increase thrust. For the secondary components, one scheme involves incorporating a material with higher electrical conductivity into specific areas of the aluminum plate, and the other involves slotting to optimize the magnetic field distribution and increase thrust. Finally, the performance of the optimized model was compared with that of the initial model. The results showed that the average thrust increased by 5.3%, while the fluctuations in thrust and normal force decreased by 13.6% and 30%, respectively, validating the effectiveness of the optimization approach.

1. INTRODUCTION

Short Primary Single-Sided Linear Induction Motor (SSLIM) features a simple structure, faster heat dissipation and lower cost than traditional rotary induction motor [1]. With the diversification of demands in the transportation sector and the rapid advancement of the technology of this motor type, it has gained widespread application across numerous fields, including industry and transportation.

Due to the end effect and large air gap of linear induction motors, their performance indicators, such as efficiency, are relatively low compared with rotary induction motors of the same capacity [2, 3]. Thrust, as a core indicator of motor output capacity, is affected by the longitudinal end effect and cogging effect, which can lead to thrust fluctuations and cause noise and vibration in the motor [4]. The unilateral linear induction motor generates a huge unilateral normal force, and the fluctuation of the normal force will impact the wheel-rail system, resulting in uneven deformation of the wheels [5].

The optimization scheme of this study includes the two ends and teeth of the primary component of the motor, while the optimization approach for the secondary component covers both structure and materials. The optimization of these various structures was performed in a progressive, step-by-step manner. Ultimately, the feasibility of the selected schemes was verified using simulation experiments.

* Corresponding author: Mingye Li (15028200250@163.com).

2. PRINCIPLE AND INITIAL ELECTROMAGNETIC CHARACTERISTICS OF LINEAR INDUCTION MOTOR

2.1. The Working Principle of a Linear Induction Motor

The basic topological structure of a short-primary single-sided linear induction motor is illustrated in Fig. 1. It consists of a primary mover and a secondary component, which comprises an aluminum plate and an iron plate.

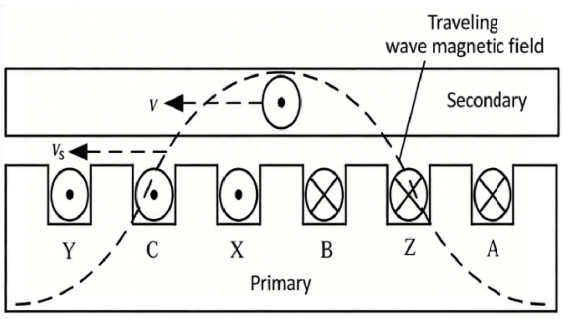

k

FIGURE 1. Working principle of SSLIM.

Because the structure of a linear induction motor is open-ended, when symmetrical three-phase alternating current is applied to the primary winding, a traveling wave magnetic field that propagates along the linear axis and exhibits a sinusoidal distribution is generated in the air gap. As the three-phase current varies sinusoidally over time, the magnetic field moves

along the linear axis at the synchronous speed v_s. In a rotating motor, the circumference of the stator is $2\pi\tau$. For a linear motor, the traveling wave magnetic field travels a distance of 2τ during one $1/f$ cycle; traveling a distance of $2\pi\tau$ requires p cycles, which is equivalent to a time of p/f. Therefore, the synchronous speed v_s can be expressed as:

$$v_s = \pi D \frac{f}{p} = 2\tau f \tag{1}$$

D corresponds to the diameter of the inner circle of the rotating motor stator; p represents the number of pole pairs; τ denotes the motor pole pitch; f indicates the power supply frequency. If the speed of the train is v, then the slip rate of the motor is s:

$$s = \frac{v_s - v}{v_s} \tag{2}$$

Based on the principle of electromagnetic induction, when the secondary aluminum plate cuts through the traveling wave magnetic field, an induced electromotive force is generated, which in turn produces an induced current in the same direction as the current in the primary Y-winding. The interaction between the secondary induced current and the traveling wave magnetic field generates an electromagnetic thrust. In actual operation, the direction of the thrust acting on the secondary component of the motor is the same as that of the traveling wave magnetic field, while the direction of the thrust acting on the primary component of the motor is opposite to that of the traveling wave magnetic field.

2.2. Initial Electromagnetic Properties

The modeling and simulation of the linear induction motor were performed using a transient solver within the ANSYS Maxwell 2D software. The primary structural parameters of the motor used to construct the model are listed in Table 1. The windings adopted a double-layer lap winding configuration.

TABLE 1. Main structural dimensions of LIM.

Parameters	Numerical Value/mm
Primary length	2010
Primary altitude	85
Primary width	220
Number of slots	80
Slot depth	41
Slot width	16.8
Slot pitch	25
Secondary aluminum plate thickness	4
Secondary iron plate thickness	36
Mechanical air gap	10

The electrical input rated parameters for the motor were set as follows: voltage of 220 V, maximum effective current value of 341 A, and rated frequency of 44 Hz. Based on these parameters, a two-dimensional finite element model of the single-sided linear induction motor is shown in Fig. 2 was established, and its initial electromagnetic characteristics are presented.

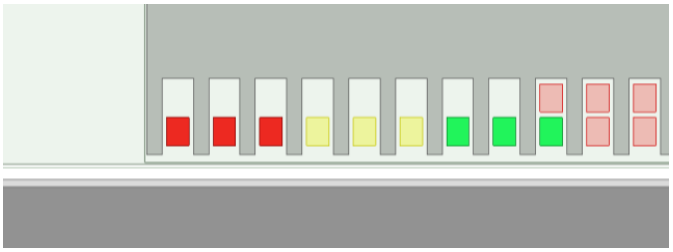

FIGURE 2. Local part of LIM's two-dimensional finite element model.

Figures 3(a) and 3(b) show the distribution of magnetic field lines under stationary conditions and when the primary and secondary primary and secondary components of the motor are moving relative to each other at a slip rate of 0.2, respectively. As can be seen from Fig. 3(a), the distribution of magnetic field lines in a linear induction motor is consistent with the theory of conventional rotating motors [6].

Figure 4 shows the magnetic flux density distribution of the motor in motion. The ends of the motor are semi-filled grooves with low magnetic flux density. The model as a whole does not exhibit saturation.

The faster the relative motion is between the primary and secondary components of the motor, the greater the rate of change in the magnetic flux within the aluminum plate, and the larger the induced eddy currents are. In addition to a certain increase in thrust, this also leads to increased eddy current losses, which in turn cause heating. Furthermore, the repulsive component of the normal force increases; if this change is uneven, it may cause the train to exert a certain impact on the wheels and rails.

The initial thrust and normal force waveforms of the model are shown in Fig. 5. Their respective initial magnitudes were a thrust of 2.48 kN and a normal force of 1.22 kN.

Figure 6 shows the no-load back EMF of the motor. The peaks of each phase are $Ea = 177.2$ V, $Eb = 188.3$ V, $Ec = 181.2$ V. Due to the disconnection of both ends of the motor, the peaks of phase A and phase C are slightly lower than that of phase B.

Figure 7 shows that the maximum value of the air gap flux density is approximately 0.425 T.

3. STRUCTURAL OPTIMIZATION OF LIM

3.1. Elementary Structural Optimization

3.1.1. Primary Iron Core Chamfer Structure

When the primary movement is in motion, the conductor plate below will induce eddy currents that weaken the magnetic field due to the sudden appearance of the magnetic field and will also induce eddy currents to maintain the magnetic field due to the sudden disappearance of the magnetic field.

Assume that the magnetic field strength B established by the primary current is a step function $b(x)$, where x is the position

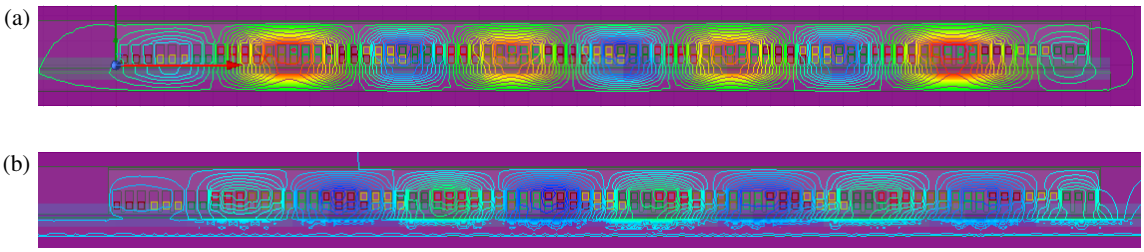

FIGURE 3. Magnetic field distribution diagram at different mover speeds. (a) Magnetic field distribution when the mover is at rest. (b) Magnetic field distribution at mover velocity of 16 m/s.

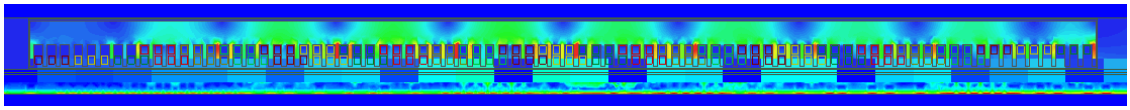

FIGURE 4. Magnetic flux density distribution in a LIM.

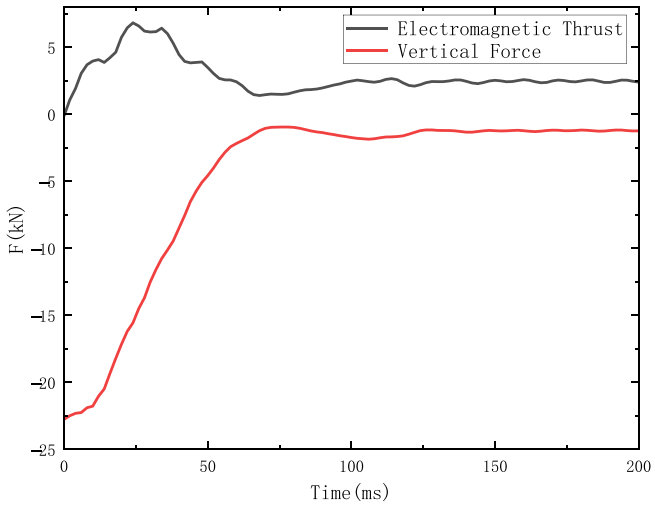

FIGURE 5. Initial values of thrust and normal force.

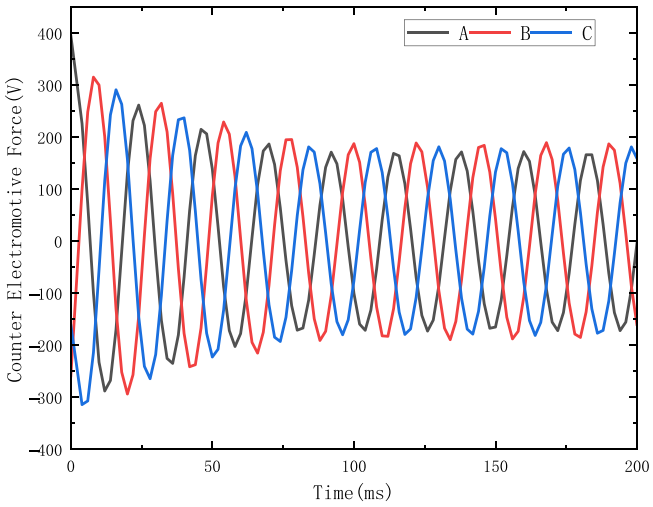

FIGURE 6. Back EMF.

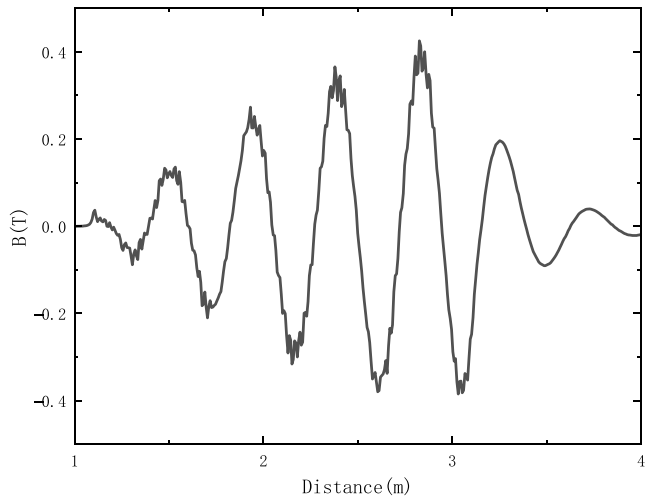

FIGURE 7. Magnetic flux density in the air gap.

along the direction of motion of the motor at the entrance:

$$b(x) = \begin{cases} 0 & x < 0 \\ B & x \geq 0 \end{cases} \tag{3}$$

The air-gapped magnetic field distribution is weakened at the inlet and strengthened at the outlet end. The magnetic field waveform is not a rectangle in its ideal state, but is distorted at both ends [7]. This distortion causes fluctuations in electromagnetic forces, which can cause vibration and noise.

The chamfered structure is set at both ends of the main core, and the original right angle is cut into a bevel at a specific angle. The design aims to smooth the magnetic field distribution at both ends while keeping the air gap body basically unchanged, essentially increasing the air gap length at the end [8]. As a result, the process of magnetic field establishment evolved from an abrupt, step-like change to a smooth, gradual transition, and L_c represents the chamfer length:

$$b(x) = \begin{cases} 0 & x < 0 \\ kx & 0 \leq x < L_c \\ B & x \geq L_c \end{cases} \tag{4}$$

Increasing the length of the air gap at both ends can smooth the transition of the magnetic circuit and effectively reduce the

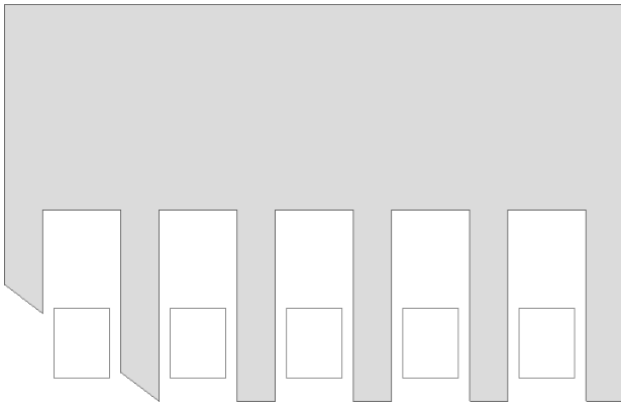

FIGURE 8. Chamfer both ends of the initial section.

interference caused by sudden changes in the magnetic field to the motor system. Given that the influence of the end effect is confined to the front and rear end regions of the primary structure, this study adopts an optimization scheme involving the construction of triangular chamfering structures at both ends of the primary structure [9]. The structural configuration is shown in Fig. 8.

To facilitate convenient modifications to the primary component of the motor within the motor model, the chamfer dimensions were selected based on the following reference values: 8.2 mm representing the tooth width and 33.2 mm representing the combined width of one slot and one tooth. The specific chamfer dimensions applied to the motor are listed in Table 2.

TABLE 2. Chamfer dimensions and angles.

Serial Number	Base Length/mm	Height/mm
1	8.2	15
2	8.2	8.2
3	33.2	25
4	33.2	33.2

Through finite element simulation, the characteristic curves of the peak-to-peak fluctuations in thrust and normal force before and after optimization were obtained, as shown in Figs. 9 and 10. In the scenario where only the base length of the chamfer structure remains unchanged while its height is varied as a reference, the magnitude of the thrust remains largely stable. As the overall size of the chamfer increases, the thrust decreases slightly, but the change is small compared to the initial value. The average thrust values ranged between 2.46 and 2.48 kN, with fluctuations deviating by no more than 20 N. In the figures, the dotted curve marked as 0 represents the original thrust and normal force variation curves of the motor, whereas the remaining curves correspond to the motor after optimization with various chamfer dimensions. The mechanical characteristic curves before and after optimization remained nearly unchanged.

The following figure presents the variation curves for the normal force. Under the chamfer structure configuration, the magnitude of the normal force was slightly reduced compared

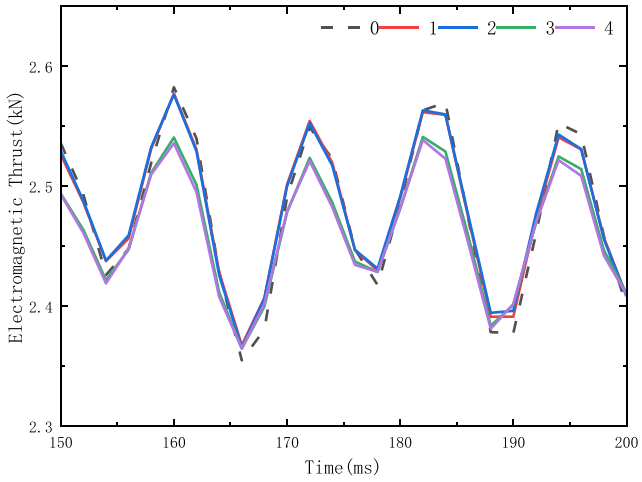

FIGURE 9. Thrust fluctuation.

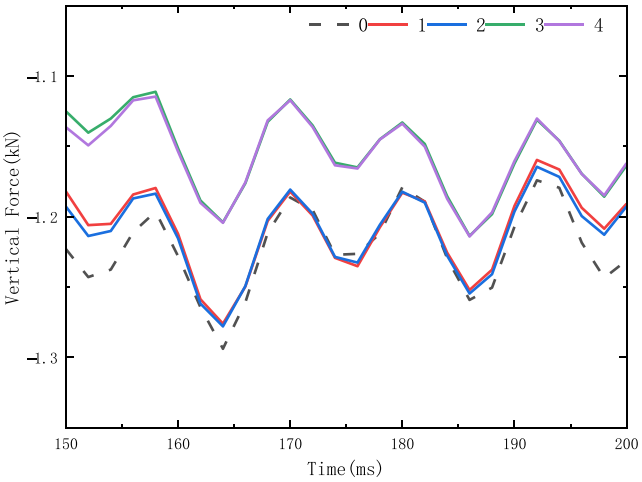

FIGURE 10. Normal force fluctuation.

to that of the original model, and the effect of reducing the fluctuation amplitude was distinctly noticeable.

The thrust fluctuation was reduced from an initial 0.22 to 0.17 kN, achieving a reduction of 22.7%. The normal force fluctuation amplitude decreased from an initial value of 0.12 to 0.09 kN, representing a reduction of approximately 25%. The results indicate that although the chamfer structure has a limited effect on increasing the magnitude of the electromagnetic force, it is highly effective in suppressing electromagnetic force fluctuations.

3.1.2. Add a Trapezoidal Structure at the Tooth End

Since the magnetic resistance of air is much higher than that of the core, when the primary and secondary stages of the motor move relative to each other, the magnetic resistance encountered by the secondary conductor will alternate between low and high, resulting in thrust fluctuations and affecting train operation.

A trapezoidal transition structure is set between the groove and the teeth to achieve a smooth transition from high to low magnetic resistance. The essence of this structure is to in-

crease the effective cross-sectional area of the magnetic circuit by widening the tooth end, so that the magnetic flux is more evenly distributed in the air gap and reduces the magnetic flux density per unit area within the tooth. As a result, the overall resistance of the motor to magnetic saturation is enhanced, allowing more effective magnetic flux to cut the conductive plate and obtain a greater thrust density under the same excitation.

Building upon the chamfer structure configured at the primary of the linear induction motor in the previous section, with dimensions of 33.2 mm in base length and 25 mm in height, this section further incorporates trapezoidal structures of varying dimensions at the bottom ends of the slots and teeth to investigate the optimization results of its electromagnetic performance under such configurations. A schematic of the added trapezoidal structure is shown in Fig. 11.

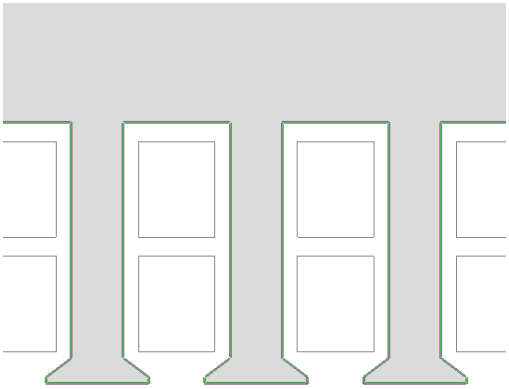

FIGURE 11. Teeth tips designed with a trapezoidal structure.

The dimensions of the trapezoidal structure adopted for the linear induction motor in this study are listed in Table 3. Keeping the length of the upper base of the trapezoid constant and ensuring a certain width for the slot opening, the height of the trapezoid was set to a fixed length of 4 mm. Only the length of the lower base was varied as a single parameter to observe the influence of this configuration on the electromagnetic force of the motor.

TABLE 3. Dimensions of different trapezoidal structures.

Top Base/mm	Bottom Base/mm	Height/mm
1	4	4
1	5	4
1	6	4
1	7	4

The corresponding structural diagram is shown in Fig. 12.

The force characteristic curves of the motor before and after optimization, obtained through a finite element simulation, are shown in Fig. 13. As the length of the lower base of the trapezoid increased, the thrust correspondingly increased, with the electromagnetic thrust increasing from 2.48 to approximately 2.59 kN, representing an increase of approximately 5%. In the figure, the dotted curve marked as 0 represents the initial thrust curve of the motor under the new configuration, and the remaining curves correspond to the motor after optimization. To observe the thrust variation more clearly, the thrust curves within the interval from 150 to 200 ms are selected and enlarged, illustrating the differences in thrust before and after optimization.

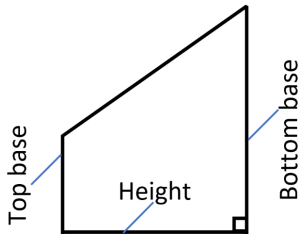

FIGURE 12. A trapezoidal structure added to the tooth section.

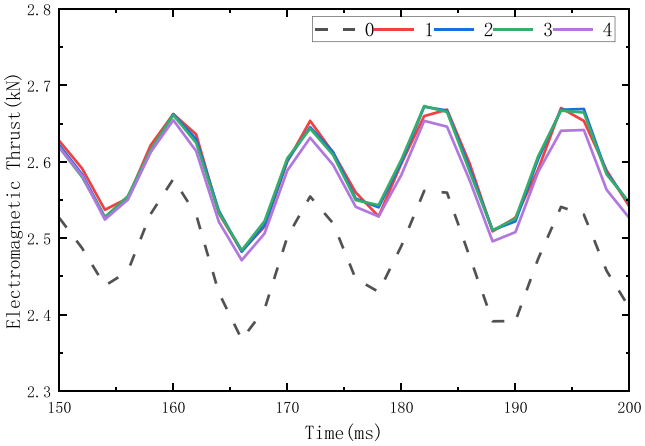

FIGURE 13. Thrust under different trapezoid sizes.

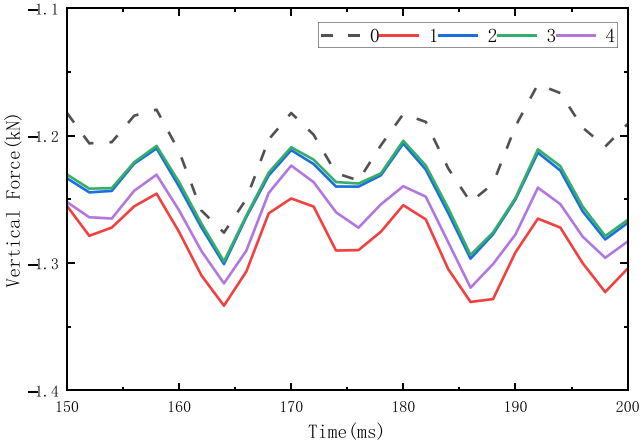

FIGURE 14. Normal force under different trapezoid sizes.

Figure 14 presents a comparison of the normal force magnitudes. By selecting the effect curves within the time segment of 150–200 ms, it can be clearly observed that the normal force after optimization significantly decreased compared to its previous state. Specifically, the normal force increased from an initial value of approximately 1.22 to 1.29 kN, representing an increase of approximately 7%.

The simulation results showed that widening the tooth tips into a trapezoidal structure can effectively enhance the motor thrust.

3.2. Secondary Structure Optimization

Building upon the optimization work previously performed on the primary structure, specifically selecting dimensions of 33.2 mm for the chamfer base length and 25 mm for its height, along with trapezoidal dimensions of 1 mm for the upper base, 4 mm for the lower base, and 4 mm for the height, this section focuses on optimizing the secondary structure.

3.2.1. Groove on the Secondary Aluminum Plate

Grooves are made in the aluminum plate to guide the eddy current path and optimize the magnetic field distribution, thus weakening the effect of the end effect [10]. Since the motor model is built in a two-dimensional plane, it is difficult to set up a longitudinal groove parallel to the direction of motor movement on the aluminum plate. Therefore, the grooves on the aluminum sheet are arranged transversely.

The principle is similar to setting up a trapezoidal structure at the tip of the tooth. The results can be observed by milling trapezoidal grooves of the same shape and size but with different spacings on the aluminum sheet, with grooves set to 5 mm, 10 mm, and 15 mm, and simulated separately for each configuration. Fig. 15 shows a slotted configuration on an aluminum plate with an iron plate on the bottom layer.

FIGURE 15. Slotted structure of secondary aluminum sheets.

The electromagnetic force characteristic curves of the motor before and after optimization, obtained through a finite element simulation, are shown in Figs. 16 and 17, respectively. As the distribution distance between the slots decreased, that is, as the slot density increased, the thrust correspondingly improved with the electromagnetic thrust rising from approximately 2.59 to 2.76 kN, representing an increase of 6.6%.

However, it was observed during the simulation that while this configuration yielded a significant effect in increasing thrust, it simultaneously elevated the magnitude of the normal force. As shown in the figures, the normal force increased from approximately 1.29 to 1.6 kN.

3.2.2. Embed Highconductivity Materials in Secondary Aluminum Plates

Thrust is essentially the traveling wave magnetic field inducing current in the secondary conductor, and the magnetic field then exerts a force on the conductor with current [11–13]. This section only briefly discusses the role of the conductivity of primary conductive materials in the generation of thrust.

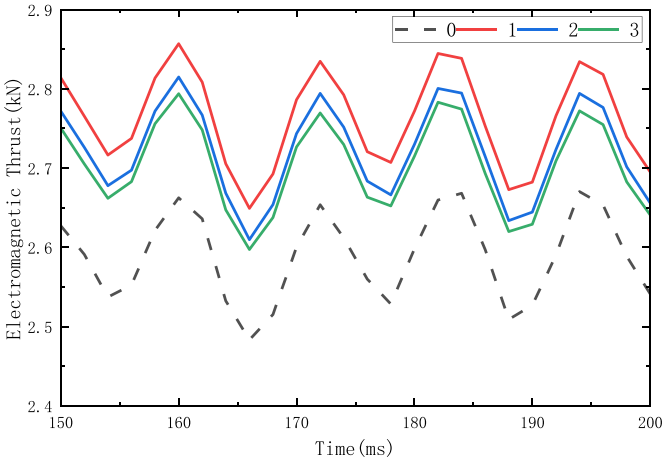

FIGURE 16. Thrust increase.

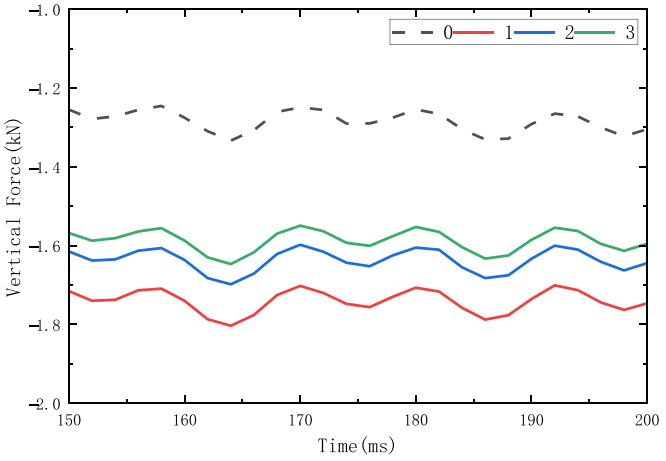

FIGURE 17. Normal force amplification.

The influence of conductivity of the secondary conductive layer on the electromagnetic field is first reflected by a dimensionless complex number λ_2 that describes the distribution of induced current and skin effect in the conductive layer, which comprehensively reflects the influence of conductivity σ_{2e}, permeability μ_2, slip s, and operating frequency on the distribution of electromagnetic fields of conductor materials:

$$\lambda_2 = \sqrt{1 + j\sigma_{2e}\mu_2 s v_s \tau/\pi} = \alpha_2 + j\beta_2 \tag{5}$$

λ_2 is the complex propagation constant that describes the propagation and attenuation characteristics of electromagnetic waves in a moving conductor. It determines how the magnetic field and induced current are distributed inside the conductor, which is the mathematical description of the "skin effect". α_2 represents the phase constant, which determines the wavelength change of the traveling wave as it propagates in the conductor; β_2 represents the attenuation constant, which determines how deep the electromagnetic field can penetrate the conductor, and the larger the β_2, the shallower the penetration, and the more significant the skin collection effect.

The overall electromagnetic effect of the composite secondary composed of a conductive layer (thickness d_2) and a back iron plate (thickness d_1) can be equivalent to a conduc-

FIGURE 18. New materials embedded in aluminum sheets.

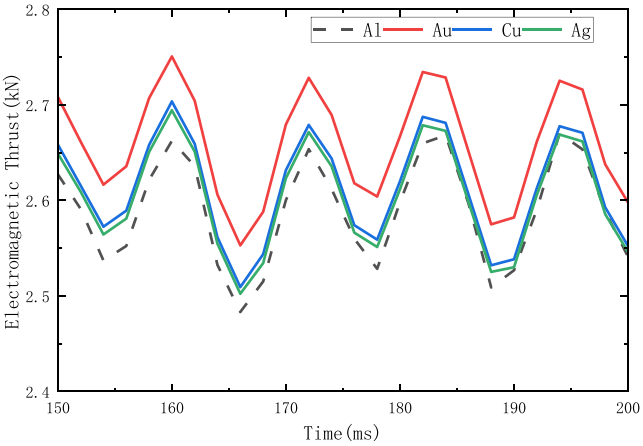

FIGURE 19. Thrust under different materials.

tive layer with complex depth $d_2\lambda_2'$, which satisfies:

$$\frac{\pi}{\tau}d_2\lambda_2' = \tanh^{-1}\left\{\frac{\mu_0}{\mu_2}\lambda_2 \tanh\frac{\pi}{\tau}(d_2\lambda_2 + d_1\lambda_1')\right\} \quad (6)$$

Analyzing this equation yields $\lambda_2' = \alpha_2' + j\beta_2'$. Among them, α_2' mainly affects the spatial attenuation distribution of the air gap magnetic field, and β_2' is directly related to the reaction magnetic field generated by the induced eddy current in the secondary plate, which is the source of thrust.

The primary traveling wave magnetic field described by J_1 interacts with the secondary described by (α_2', β_2'), resulting in an electromagnetic thrust F as:

$$F = \frac{1}{2}\mu_0 J_1^2 \frac{\sin 2\frac{\pi}{\tau}d_2\beta_2'}{\cosh 2\frac{\pi}{\tau}(g_e + d_2\alpha_2') - \cos 2\frac{\pi}{\tau}d_2\beta_2'}(2h\tau p) \quad (7)$$

μ_0: vacuum permeability; J_1: the amplitude of the primary surface current density, which represents the excitation size of the armature current; g_e: equivalent electromagnetic air gap corrected by Carter coefficient; τ: pole distance; h, p: the stack thickness and pole logarithm of the primary core; the product $2h\tau p$ represents the effective working area of the motor; $\sin 2\frac{\pi}{\tau}d_2\beta_2'$ indicates that the magnitude of thrust is directly controlled by β_2', and under the approximate conditions of low slip and a thin conductive layer, the relationship can be simplified to $\beta_2' \propto \sigma_{2e}s$, and the higher the conductivity of the material, the greater the thrust generated under the same slip.

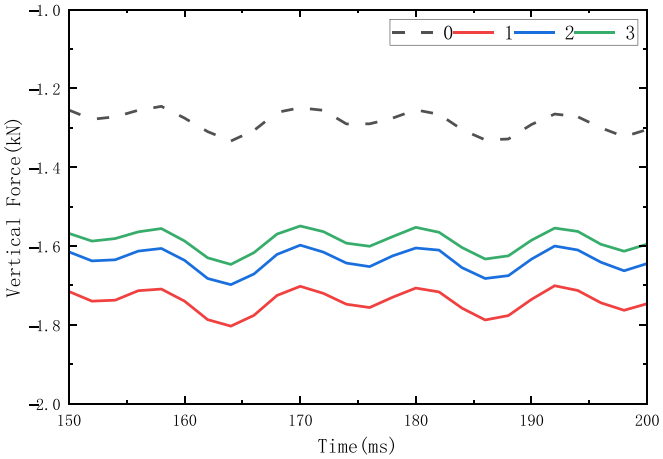

FIGURE 20. Normal force under different materials.

Given that the electrical conductivity of the aluminum plate selected for the linear induction motor is approximately $3.8 * 10^7$ S/m, the possibility of slotting the aluminum plate to embed other materials with higher electrical conductivity than aluminum is considered to observe the effect on motor performance. The experimental approach adopted in this study involved milling rectangular grooves into an aluminum plate at intervals of 6 mm. Each groove had a depth of 1 mm and a width of 2 mm. These grooves are subsequently filled with materials exhibiting electrical conductivities higher than that of aluminum. The electrical conductivities of the new materials injected into the grooves milled into the aluminum plate are presented in Table 4.

TABLE 4. Electrical conductivity of materials.

Materials	Electrical Conductivity S/m
Al	$3.77 * 10^7$
Au	$4.52 * 10^7$
Cu	$5.80 * 10^7$
Ag	$6.30 * 10^7$

The embedded structure of the motor secondary aluminum plate is illustrated in Fig. 18.

By conducting electromagnetic simulation experiments on the aforementioned embedded structures with materials of different electrical conductivities, variations in the electromagnetic characteristics of the motor under different embedded materials were observed. The characteristic curves of the electromagnetic force for the optimized motor are shown in Figs. 19 and 20. Evidently, as the electrical conductivity of the injected material increased, the thrust increased from 2.59 kN to approximately 2.66 kN, representing an increase of 2.7%.

However, the normal force increased from approximately 1.29 to 1.53 kN, representing an increase of approximately 18.6%.

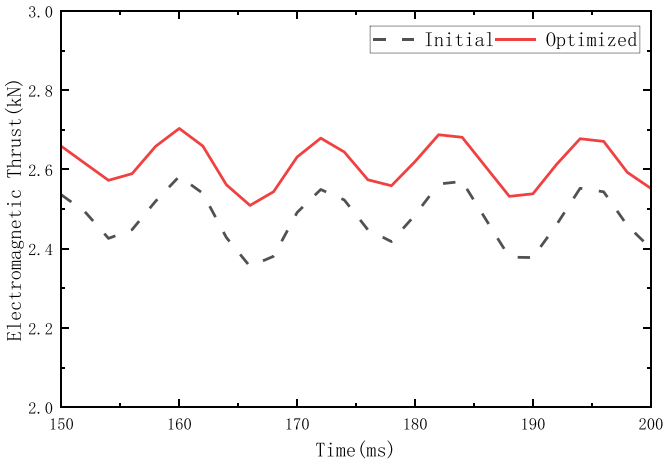

FIGURE 21. Thrust comparison.

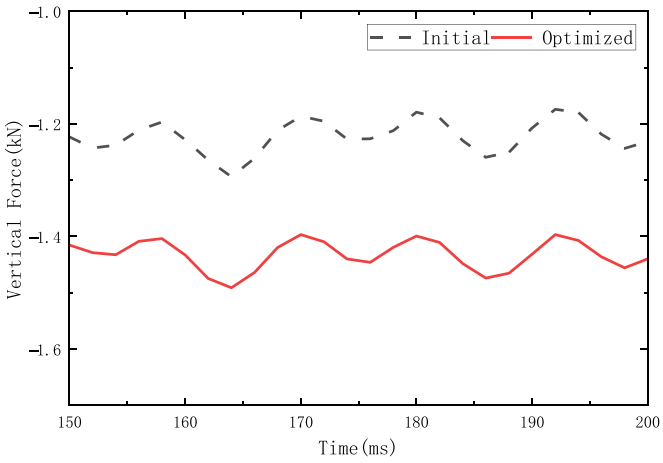

FIGURE 22. Comparison of normal forces.

4. COMPARISON OF INITIAL AND OPTIMIZED MODEL FEATURES

To observe the optimization results of the selected scheme for the linear induction more clearly, this study compares the electromagnetic characteristics of the initial model with those of the optimized model. Since the optimization results of the two secondary-side schemes partially overlap, the method with better performance — the interlocking structure — was selected. The final optimized model incorporated a chamfer structure with dimensions of 33.2 mm (base length) and 25 mm (height), a trapezoidal structure with dimensions of 1 mm (upper base), 4 mm (lower base), and 4 mm (height), and copper, a high-conductivity material, injected into the secondary.

A comparison between the two models is presented in the following section, demonstrating significant improvements in various electromagnetic characteristics. Fig. 21 shows that the average electromagnetic thrust of the motor increased from 2.48 kN in the initial model to 2.61 kN, representing an increase of approximately 5.3%; specifically, the fluctuation amplitude decreased from 0.22 to 0.19 kN, achieving a reduction of 13.6%.

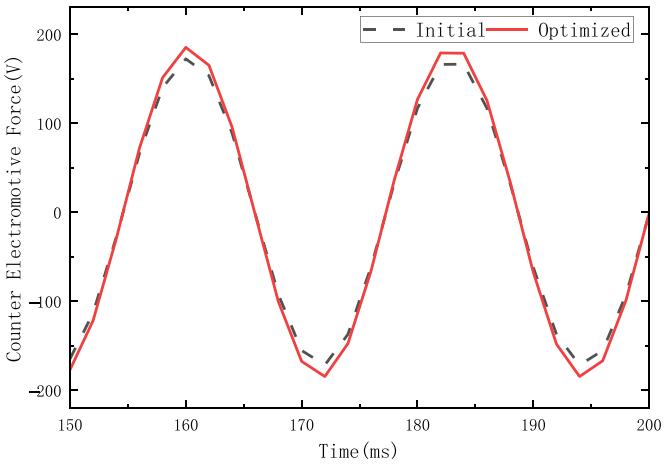

FIGURE 23. Comparison of counter-EMF.

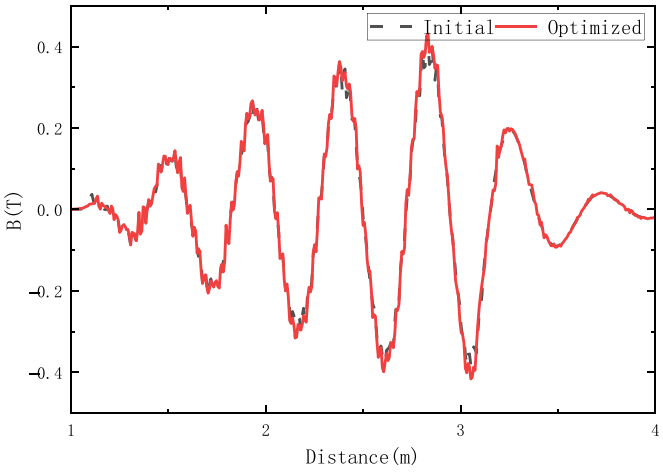

FIGURE 24. Comparison of magnetic flux density in the air gap.

Figure 22 shows that the average normal force of the motor increased from 1.22 kN in the initial model to 1.43 kN, representing an increase of approximately 17.2%; the fluctuation amplitude decreased from 0.13 to 0.09 kN, achieving a reduction of 30%.

Taking phase A as an example, Fig. 23 shows that the back-EMF increased from 172.2 V to 185.1 V.

Figure 24 shows that the maximum value of the air-gap flux density increased from 0.425 to 0.431 T.

TABLE 5. Comparison of the characteristics of the initial model and the final optimized model.

Characteristic	Initial Model	Final Optimized Model
Thrust/kN	2.48	2.61
Thrust Amplitude/kN	0.22	0.19
Normal Force/kN	1.22	1.43
Normal Force Amplitude/kN	0.13	0.09
Back-EMF/V	172.2	185.1
Air-Gap Flux Density/T	0.425	0.431

The comparison between the initial model of the motor and the model after the final application of the selected optimization scheme is shown in Table 5.

5. CONCLUSION

In this study, specific optimizations were performed on the primary and secondary structures of a single-sided linear induction motor, successfully achieving the primary objectives of enhancing motor thrust and reducing force fluctuations. To optimize the primary structure, schemes involving chamfering and a trapezoidal tooth configuration were adopted. The experimental results show that implementing a chamfer structure on the primary component of the motor effectively suppresses fluctuations in both the thrust and normal force, whereas adding a trapezoidal structure to the tooth tips of the primary component of the motor significantly increases the electromagnetic thrust. Regarding the optimization of the secondary structure, methods such as injecting high-conductivity materials and creating slots have been employed. Ultimately, the scheme involving the injection of high-conductivity materials was selected for incorporation into the final optimized model.

The final results indicate that, compared with the initial model, the average thrust, a key parameter, increased by 5.3%, whereas the thrust fluctuations decreased by 13.6%. The average normal force increased by 17.2%, but its fluctuation amplitude decreased by 30%. This reduction in normal force fluctuation is beneficial for mitigating the impact on the wheel-rail system of the train. The effectiveness of the adopted optimization schemes was successfully validated through finite element simulation experiments conducted on the aforementioned structural optimization methods.

REFERENCES

[1] Jiang, Z., T. Xu, J. Qian, L. Huang, H. Xu, X. Wang, and J. Lou, "Structural optimization of linear induction motor for reducing end effect," in *2020 IEEE 9th International Power Electronics and Motion Control Conference (IPEMC2020-ECCE Asia)*, 1998–2001, Nanjing, China, 2020.

[2] De Oliveira, R. A. H., F. J. G. Trad, F. S. Costa, R. M. Stephan, A. C. Ferreira, and I. E. Chabu, "Double-primary with segmented-secondary linear induction motor for mining industry conveyor systems," *IEEE Transactions on Industrial Electronics*, Vol. 72, No. 12, 12 481–12 490, 2025.

[3] Ahmadpour, A., A. Dejamkhooy, and H. Shayeghi, "Design and force analysis of salient single-sided linear induction motor," *Electric Power Components and Systems*, Vol. 49, No. 1-2, 184–198, 2021.

[4] Shin, J.-S., R. Watanabe, T. Koseki, H.-J. Kim, and Y. Takada, "The design for cogging force reduction of a double-sided transverse flux permanent magnet linear synchronous motor," *IEEE Transactions on Magnetics*, Vol. 50, No. 11, 1–4, 2014.

[5] Jiang, Z., "Research on normal force of linear induction motor based on ansoft," in *2024 3rd International Conference on Energy and Electrical Power Systems (ICEEPS)*, 1018–1021, Guangzhou, China, 2024.

[6] Li, T., L. Shi, P. Wang, and Z. Li, "Fast magnetic field analysis method for long primary double-sided linear induction motors with slot considered," in *2024 8th International Conference on Power and Energy Engineering (ICPEE)*, 23–28, Chengdu, China, 2024.

[7] Lv, G., T. Zhou, and D. Zeng, "Influence of the V-type secondary on the air-gap magnetic field and performance of the linear induction motor," *IET Electric Power Applications*, Vol. 13, No. 2, 229–234, 2019.

[8] Lee, H.-W., C.-B. Park, and B.-S. Lee, "Thrust performance improvement of a linear induction motor," *Journal of Electrical Engineering & Technology*, Vol. 6, No. 1, 81–85, 2011.

[9] Yamaguchi, H. and M. Morishita, "End effects of Halbach field magnet-type linear motor," *Electrical Engineering in Japan*, Vol. 216, No. 4, e23450, 2023.

[10] Naderi, P., M. Heidary, and M. Vahedi, "Performance analysis of ladder-secondary-linear induction motor with two different secondary types using magnetic equivalent circuit," *ISA Transactions*, Vol. 103, 355–365, 2020.

[11] Lv, G., Q. Li, Z. Liu, Y. Fan, and G.-G. Li, "The analytical calculation of the thrust and normal force and force analyses for linear induction motor," in *2008 9th International Conference on Signal Processing*, 2795–2799, Beijing, China, 2008.

[12] Shiri, A., "Electromagnetic force analysis in linear induction motors, considering end effect," in *2016 7th Power Electronics and Drive Systems Technologies Conference (PEDSTC)*, 105–110, Tehran, Iran, 2016.

[13] Zhou, W., Z. Sun, F. Cui, and Y. Mao, "Electromagnetic design of high-speed and high-thrust cross-shaped linear induction motor," *IEEE Access*, Vol. 9, 87 501–87 509, 2021.